RSC Advances

PAPER

View Article Online
View Journal | View Issue

Cite this: *RSC Adv.*, 2019, **9**, 30671

Impact of La^{3+} and Y^{3+} ion substitutions on structural, magnetic and microwave properties of $Ni_{0.3}Cu_{0.3}Zn_{0.4}Fe_2O_4$ nanospinel ferrites synthesized *via* sonochemical route

M. A. Almessiere, *[ab] Y. Slimani, *[a] A. Demir Korkmaz,[c] A. Baykal,[d] H. Güngüneş,[e] H. Sözeri,[f] Sagar E. Shirsath,[g] S. Güner,[h] S. Akhtar[a] and A. Manikandan[i]

In the current study, $Ni_{0.4}Cu_{0.2}Zn_{0.4}La_xY_xFe_{2-x}O_4$ (x = 0.00 − 0.10) nanospinel ferrites (NSFs) were fabricated *via* an ultrasonic irradiation route. The creation of single phase of spinel nanoferrites (NSFs) was investigated by X-ray powder diffractometry (XRD) and selected area diffraction pattern (SAED). The cubic morphology of all samples was confirmed by scanning and transmission electron microscopies (SEM and TEM) respectively. The UV-Vis investigations provided the direct optical energy band gap values in a narrow photon energy interval of 1.87–1.92 eV. The ^{57}Fe Mössbauer spectroscopy analysis explained that the hyperfine magnetic fields of Octahedral (Oh) and Tetrahedral (Td) sites decreased with substitution. The paramagnetic properties of NPs decrease with increase of content of doped ions. Investigations of magnetic properties reveal a superparamagnetic nature at 300 K and soft ferromagnetic trait at 10 K. The M_s (saturation magnetization) and M_r (remanence) decrease and the H_c (coercivity) increases slightly with La^{3+} and Y^{3+} substitution. The observed magnetic traits are deeply discussed in relation with the morphology, structure, magnetic moments and cation distributions. The microwave characterization of the prepared NSFs showed that, dissipation (*i.e.*, absorption) of incoming microwave energy occurs at a single frequency, for each sample, lying between 7 and 10.5 GHz. The reflection losses (RL) at these frequencies range from −30 to −40 dB and the mechanism of which is explained in the framework of dipolar relaxation and spin rotation. The best microwave properties were obtained with a LaY concentration of x = 0.08 having an RL of −40 dB @ 10.5 GHz and an absorption bandwidth of 8.4 GHz @ −10 dB. With these high values of RL and absorbing bandwidth, LaY doped NiCuZn NSF products would be promising candidates for radar absorbing materials in the X-band.

Received 14th August 2019
Accepted 19th September 2019

DOI: 10.1039/c9ra06353f

rsc.li/rsc-advances

1. Introduction

Nanocrystalline spinel ferrites (NSFs) are promising materials in the few last decades because of their unique electrical and magnetic features including high resistivity, high Curie temperature, high saturation magnetization and low eddy current loss. Thus, NSFs have found a considerable amount of use in environmental, biomedical, industrial and technological applications including magnetic resonance imaging microwave absorbers, contrast agents, catalysts, drug delivery agents, magnetic storage devices *etc.*[1–9] Ni–Cu–Zn ferrite is a spinel ferrite mainly used in multi-layer chip inductors (MLCIs).[10] MLCIs are mainly used in mobile phones, notebook computers and video cameras. MLCIs are produced with alternating layers of silver electrodes and spinel ferrites. For further miniaturization of these devices, it is important to obtain fewer layers with high efficiency. Therefore, NiCuZn ferrites can be tuned with diverse substitution contents and/or various metal ions to produce a product with high resistivity, low coercivity, high

[a]*Department of Biophysics, Institute for Research & Medical Consultations (IRMC), Imam Abdulrahman Bin Faisal University, P. O. Box 1982, Dammam, 31441, Saudi Arabia. E-mail: malmessiere@iau.edu.sa; yaslimani@iau.edu.sa*

[b]*Department of Physics, College of Science, Imam Abdulrahman Bin Faisal University, P. O. Box 1982, Dammam, 31441, Saudi Arabia*

[c]*Department of Chemistry, Istanbul Medeniyet University, 34700 Uskudar, Istanbul, Turkey*

[d]*Department of Nanomedicine, Institute for Research & Medical Consultations (IRMC), Imam Abdulrahman Bin Faisal University, P. O. Box 1982, Dammam, 31441, Saudi Arabia*

[e]*Department of Physics, Hitit University, 19030, Çevre Yolu Bulvarı, Çorum, Turkey*

[f]*TUBITAK-UME, National Metrology Institute, P. O. Box 54, 41470 Gebze-Kocaeli, Turkey*

[g]*School of Materials Science and Engineering, University of New South Wales, Kensington, Sydney, NSW 2052, Australia*

[h]*Institute of Inorganic Chemistry, RWTH Aachen University, D-52074 Aachen, Germany*

[i]*Department of Chemistry, Bharath Institute of Higher Education and Research (BIHER), Bharath University, Chennai, 600073, Tamil Nadu, India*

permeability and low dielectric constant.[11] In Ni–Cu–Zn spinel lattice, Cu^{2+} and Ni^{2+} ions prefer to occupy the Oh sites, Zn^{2+} ions occupied the Td sites, and Fe^{3+} ions occupied both Oh (A) and Td (B) sites partially. The A–A, B–B and A–B superexchange interactions are responsible for magnetization in spinel ferrites.[12] Consequently, the saturation magnetization of a spinel ferrite can be tuned by the various metal ion substitution.

Rare earth elements present a novel approach for obtaining NSFs desired characteristics for MLCI applications as well as other uses. Rare earth metal ions whose ionic radii are greater than that of the iron(III) ion, micro-strains will be established in the spinel ferrite crystal structure. Micro-strains will trigger a domain wall motion which will result with a deformation in the lattice cell. The domain wall motion and the spin rotational magnetization within the domains are responsible for the permeability. In fact, lower amounts of dopants may stabilize the microstructure while higher concentrations which are above the solubility limit may cause a non-uniform grain size.[13] Therefore, the rare earth substitution of NSFs can result in enhanced permeability when the substituting ratio is small. In addition, rare earth metal ions are known to enhance the optical properties of ferrites. For example, the incorporation lanthanum(III) to $ZnFe_2O_4$ nanoparticles increased the optical band gap (E_g) from 1.87 eV to 1.97 eV.[14] Magnetite nanoparticles doped with Dy, Nd, or La were found the display direct gap values of 3.2–3.55 eV and indirect band gap values of 1.1–1.25 eV when compared to a direct E_g of 2.25 eV and indirect E_g of 0.9 eV in pure magnetite samples.[15]

Many different synthesis methods have been sued for Ni–Cu–Zn spinel ferrites synthesis. For example, Hu and Yan[16] applied a ball-milling technique to synthesize $(Ni_{0.17}Zn_{0.63}Cu_{0.20})Fe_{1.915}O_4$, a Ni–Zn ferrite with copper (CuO) and vanadium (V_2O_5) addition. The sintering temperature decreased and the granularity of the particles was reduced by the addition of Cu^{2+} and V^{5+} to the ferrite while an enhanced permeability was obtained since the domain wall motion was improved by higher density and bigger grain. Kabbur *et al.*[17] used a glycine-assisted sol–gel combustion for $Ni_{0.25-x}Mg_xCu_{0.30}Zn_{0.45}Fe_2O_4$ synthesis. Although the magnetic moments and the saturation magnetization values had fluctuations as the amount of magnesium ion increased, the substitution of nickel and magnesium resulted in an increase in the electrical resistivity and the sample where the Mg^{2+} content was $x = 0.15$ displayed the minimum dielectric loss tangent. In another study by Krishnaveni and co-workers,[18] $Ni_{0.53}Cu_{0.12}Zn_{0.35}Fe_2O_4$ nanopowders were obtained by microwave-hydrothermal synthesis technique and MLCIs were fabricated with nanoparticles annealed between 600–950 °C temperatures. The sample sintered at 900 °C for 4 h displayed the highest resistance, initial permeability, and inductance. Al-substituted Ni–Cu–Zn ferrites were fabricated by ceramic method in a study done by Eltabey *et al.*[19] As the aluminum ion concentration increased, the initial permeability, magnetization, and the dc resistivity were also found to increase. Finally, $Ni_{0.4}Cu_{0.2}Zn_{0.4}Fe_2O_4$ nanoparticles were obtained by a sono-chemically-assisted co-precipitation.[20] When a high-powered ultrasonic wave is applied to irradiate a liquid, several radially oscillating bubbles with micron sizes are formed.[21] This is called as acoustic cavitation. The ultrasonic wave's pressure oscillation causes the bubbles keep expanding and contracting violently. Among various methods, ultrasound irradiation assisted synthesis has many advantages such as low to no agglomeration of particles, the need for less induction time, higher number of crystals at equal supersaturation and the ability to control the particle size.[20]

In the literature, there are a limited number of reports available on the synthesis of rare-earth substituted Ni–Cu–Zn nanospinel ferrites *via* sonochemical. No reports have been published on the preparation of Ni–Cu–Zn nanospinel ferrites substituted with lanthanum and yttrium ions simultaneously. Therefore, we reported the synthesis of $Ni_{0.3}Cu_{0.3}Zn_{0.4}La_xY_xFe_{2-2x}O_4$ ($x = 0.0 - 0.10$) NSFs *via* ultrasonic irradiation. The structure, morphology, magnetic and microwave characteristics were investigated.

2. Experimental details

The $Ni_{0.3}Cu_{0.3}Zn_{0.4}La_xY_xFe_{2-2x}O_4$ ($x = 0.0 - 0.10$) NSFs were synthesized using ultrasonic irradiation procedure. The following grade precursors (sigma Aldrich) of $Ni(NO_3)_2\cdot 6H_2O$, $Cu(NO_3)_2\cdot 3H_2O$, $Fe(NO_3)_3\cdot 9H_2O$, $Zn(NO_3)_2\cdot 6H_2O$, $La(NO_3)_3\cdot 6H_2O$, $C_6H_8O_7$ and Y_2O_3 are used as initial materials. Firstly, Y_2O_3 was solved in 15 ml of concentrated HCl at 150 °C until became a clear solution. The nitrites with citric acid are dissolved in 60 ml of DI water then mixed with dissolved Y_2O_3 under stirring. A dropwise of 2 M NaOH solution has been used to set the pH at 11. The solution was undergone to ultrasonic irradiation *via* UZ SONOPULS HD2070 homogenizer (20 kHz and 70 W) for 1 h. Then, the solution containing solid product was washed with DI water. The solid part was separated by means of external magnet and dried at 80 °C.

The phase analysis has been done through Rigaku Benchtop Miniflex X-ray diffraction (XRD) with CuKα radiation. The morphology, size and chemical compositions were performed using FEI Teneo scanning electron microscope (SEM) equipped with an EDX detector and a transmission electron microscopy (TEM; FEI Morgagni 268). UV-visible diffuse reflectance (DR%) spectra were recorded in the range of 200–800 nm. MagLab instrument was used for Mössbauer analysis of samples. The quantum design coupled with VSM was utilized for magnetic characterization of samples.

3. Results and discussion

3.1. Structural analysis

The phase identification of the mixed $Ni_{0.4}Cu_{0.2}Zn_{0.4}La_xY_xFe_{2-x}O_4$ ($x = 0.00 - 0.10$) NSFs was performed in Fig. 1. NiCuZn spinel ferrite phase has been confirmed without presence of any impurities. The diffraction lines (220), (311), (222), (400), (422), (511) and (440) well accord with the single phase of spinel ferrite. Rietveld refinement of XRD experimental data was employed through full proof software to estimate the lattice parameters (Table 1). The average crystallites size was calculated through Debye–Scherrer equation (Table 1). The lattice

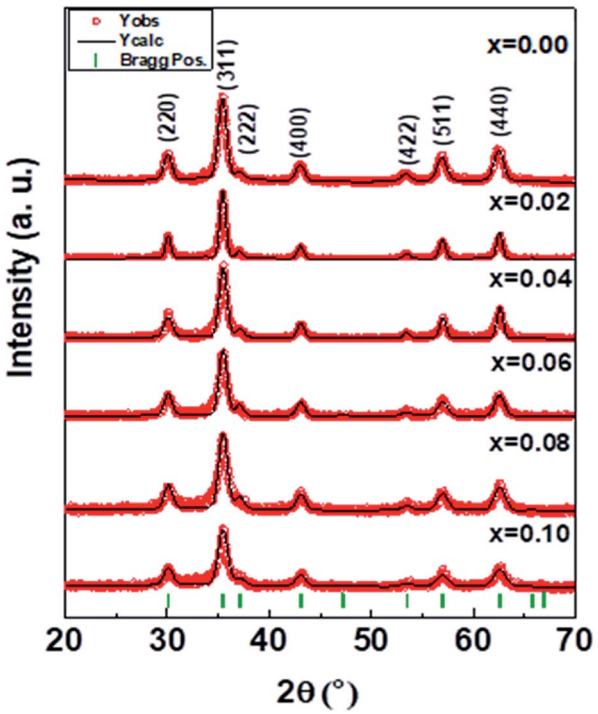

Fig. 1 XRD powder patterns of $Ni_{0.4}Cu_{0.2}Zn_{0.4}La_xY_xFe_{2-x}O_4$ ($x = 0.00 - 0.10$) NSFs.

parameter '*a*' increased with increasing the La–Y content. This is attributable to the distortion of the crystal structure caused by the occupation of octahedral sites by large ionic radii of La^{3+} and Y^{3+} substitution ions. The average crystallites size slightly decreases from about 23 to 12 nm with the increase of La–Y concentration.

Bertaut method has been employed to estimate the cations distribution of all the prepared samples by analyzing XRD patterns.[22,23] As it was given in the literature, M^{+3} and M^{+2} cation distributions among the Td and Oh sites were estimated from the intensity ratio of I_{220}/I_{440} and I_{422}/I_{400} planes. Therefore, these planes were used in the cation distribution calculations.[23] The estimated cations distribution is listed in Table 2. It has been noticed that Fe^{3+} ions occupy both Td and Oh sites. Rare-earth La^{3+} ions occupied Oh (B)-site since they have higher ionic radii whereas Y^{3+} ions occupied Td (A)-site. Zn^{2+} occupied the Td (A-site) and on the other hand Cu^{2+} and Ni^{2+} ions occupied the Oh (B)-site. This is consistent with the literature reports.[24,25]

Table 1 Refined structural parameters for $Ni_{0.4}Cu_{0.2}Zn_{0.4}La_xY_xFe_{2-x}O_4$ ($x = 0.00 - 0.10$) NSFs

x	a (Å)	V (Å)^3	D_{XRD} (nm) ± 0.04	χ^2 (chi^2)	R_{Bragg}
0.00	8.397(4)	592.14	22.8	1.36	2.73
0.02	8.398(5)	592.39	21.6	1.78	1.90
0.04	8.406(7)	594.12	20.6	1.56	5.96
0.06	8.408(6)	594.52	17.3	1.47	5.36
0.08	8.410(4)	594.90	16.8	1.24	5.17
0.10	8.416(0)	596.09	12.4	1.25	2.41

Table 2 Cation distribution of $Ni_{0.4}Cu_{0.2}Zn_{0.4}La_xY_xFe_{2-x}O_4$ ($x = 0.00 - 0.10$) NSFs

x	Tetrahedral A-site	Octahedral B-site
0.00	$Zn_{0.4}Ni_{0.05}Fe_{0.55}$	$Ni_{0.35}Cu_{0.2}Fe_{1.45}$
0.02	$Zn_{0.4}Y_{0.02}Fe_{0.58}$	$Ni_{0.4}Cu_{0.2}La_{0.02}Fe_{1.38}$
0.04	$Zn_{0.4}Y_{0.04}Fe_{0.56}$	$Ni_{0.4}Cu_{0.2}La_{0.04}Fe_{1.36}$
0.06	$Zn_{0.4}Y_{0.06}Fe_{0.54}$	$Ni_{0.4}Cu_{0.2}La_{0.06}Fe_{1.34}$
0.08	$Zn_{0.4}Y_{0.08}Fe_{0.52}$	$Ni_{0.4}Cu_{0.2}La_{0.08}Fe_{1.32}$
0.10	$Zn_{0.4}Y_{0.1}Fe_{0.50}$	$Ni_{0.4}Cu_{0.2}La_{0.1}Fe_{1.30}$

3.2. Morphological investigations

The surface morphology of $Ni_{0.4}Cu_{0.2}Zn_{0.4}La_xY_xFe_{2-x}O_4$ ($x = 0.00 - 0.10$) NSFs is offered in Fig. 2. High magnification SEM images revealed smaller grains with size in the range of few tens nanometer.[26] These grains are agglomerated due to the magnetic nature of prepared samples. EDX and elemental mapping results (Fig. 3) did not disclose any preferential segregation of heavy elements, indicating a homogeneous chemical composition. They confirmed the presence of different elements of Ni, Cu, Zn, La, Y, Fe and O and proved the formation of the desired compositions. TEM images, selected area electron diffraction (SAED) pattern and size histograms of the $x = 0.02$ and 0.06 compositions are presented in Fig. 4.

They indicated a size distribution ranging between 10 and 35 nm, and the average grains size is around 20 nm. The estimated sizes agreed very-well with the crystallites size deduced from XRD. SAED patterns revealed the well crystalline nature of the particles as confirmed by the well-separated continuous rings. The first five rings of the SAED patterns were identified as (220), (311), (400), (511) and (440). The maximum intensity was obtained for (311) reflection which is consistent with the XRD pattern.[27]

3.3. Optical properties

Optoelectronic properties of $Ni_{0.4}Cu_{0.2}Zn_{0.4}La_xY_xFe_{2-x}O_4$ ($x = 0.00 - 0.10$) NSFs were investigated *via* percent diffuse reflectance (DR%) measurements in the UV-Vis region of electromagnetic spectrum, Fig. 5. The spectrophotometer swept a photon energy range from 1.55 eV to 6.2 eV with a corresponding wavelength interval from 800 nm to 200 nm. Recorded graphs from all NiCuZn mixed ferrite samples reflect the incident radiation with the magnitudes between 26–31% in a sweep region of 200–500 nm. In the same sweep region, non-ion substituted $Ni_{0.4}Cu_{0.2}Zn_{0.4}Fe_2O_4$ nanoparticle sample has reflectance average of 30%. A sharp increase is detected at DR% values at all spectra until maximum 71% in the following sweep range. Scientific facts to use DR% spectra to specify the optical energy band gap of powder samples is correlated with the Kubelka–Munk theory. In the theory, Kubelka–Munk function (KM) is directly proportional to absorption coefficient, α

$$KM = \frac{(1 - R_\infty)^2}{2R_\infty} = \frac{2.303\varepsilon C}{S} = \alpha$$

here, R_∞ is absolute remittance, ε is absorptivity, S is twice the scattering coefficient, C is analyte concentration. Optical energy

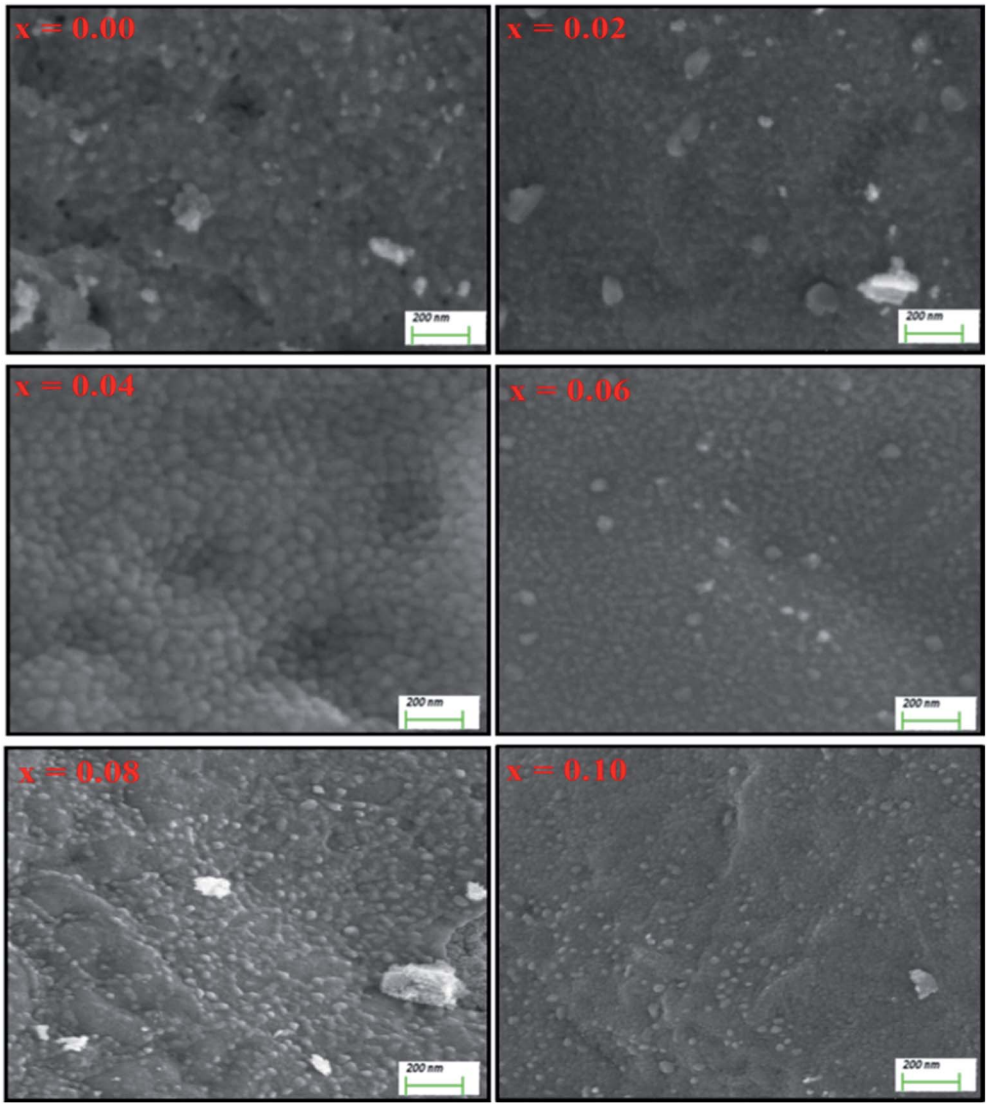

Fig. 2 SEM images of various $Ni_{0.4}Cu_{0.2}Zn_{0.4}La_xY_xFe_{2-x}O_4$ ($x = 0.00 - 0.10$) NSFs.

band gap (E_g) values are estimated applying Tauc and Davis-Mott model that provides another equation between α and E_g as below:[28–30]

$$(\alpha h\nu) = A\left(h\nu - E_g\right)^{\frac{1}{n}}$$

where h is Planck's constant, ν is frequency of incident radiation and A is a proportionality constant. Further, power n specifies that electronic transitions are indirect or direct and also in-allowed or allowed. Magnitude of n equals to 1/2 for a direct and allowed transition. Direct E_g values for all $Ni_{0.4}Cu_{0.2}Zn_{0.4}La_xY_xFe_{2-x}O_4$ ($x = 0.00 - 0.10$) were determined by extrapolating the strait line segment of Tauc plots to $(\alpha h\nu)^2 = 0$ and were given in Fig. 6. Non-ion substituted mixed spinel $Ni_{0.4}Cu_{0.2}Zn_{0.4}Fe_2O_4$ has 1.87 eV band gap. Substitution of La^{3+} and Y^{3+} ions with equal concentrations of $x = 0.02 - 0.10$ caused slight increments from this magnitude. All ion-substituted NPs have direct E_g magnitudes between minimum 1.88 eV ($x = 0.10$) and maximum 1.92 eV ($x = 0.04$). In the literature, the single reported E_g data from Tm substituted NiCuZn NSFs produced by ultrasound irradiations belongs to our group. E_g magnitudes are around 1.90 eV again.[31] However, George *et al.* also reports very close values just below 2 eV for Ce^{3+} substituted Ni–Zn mixed ferrite.[32]

3.4. Mössbauer spectra

Room-temperature Mössbauer spectra of $Ni_{0.4}Cu_{0.2}Zn_{0.4}La_xY_xFe_{2-x}O_4$ ($x = 0.00 - 0.10$) NSFs are depicted in Fig. 7 and the fitted parameters are presented in Table 3. The fitting was performed by means of three sextets, A for Td sites and B_1 and B_2 for Oh sites for undoped sample. For the doped samples, the paramagnetic doublet derived from superparamagnetic Fe^{3+} species is additionally formed. The area of this doublet increased from 9.102% to 50.126% as La^{3+} and Y^{3+} concentration increases from 0.02 to 0.10. The Fe^{3+} ions in A-site are characterized by small isomer shift (I.S.) and large hyperfine field (H_f), whereas Fe^{3+} ions in B-site are represented by

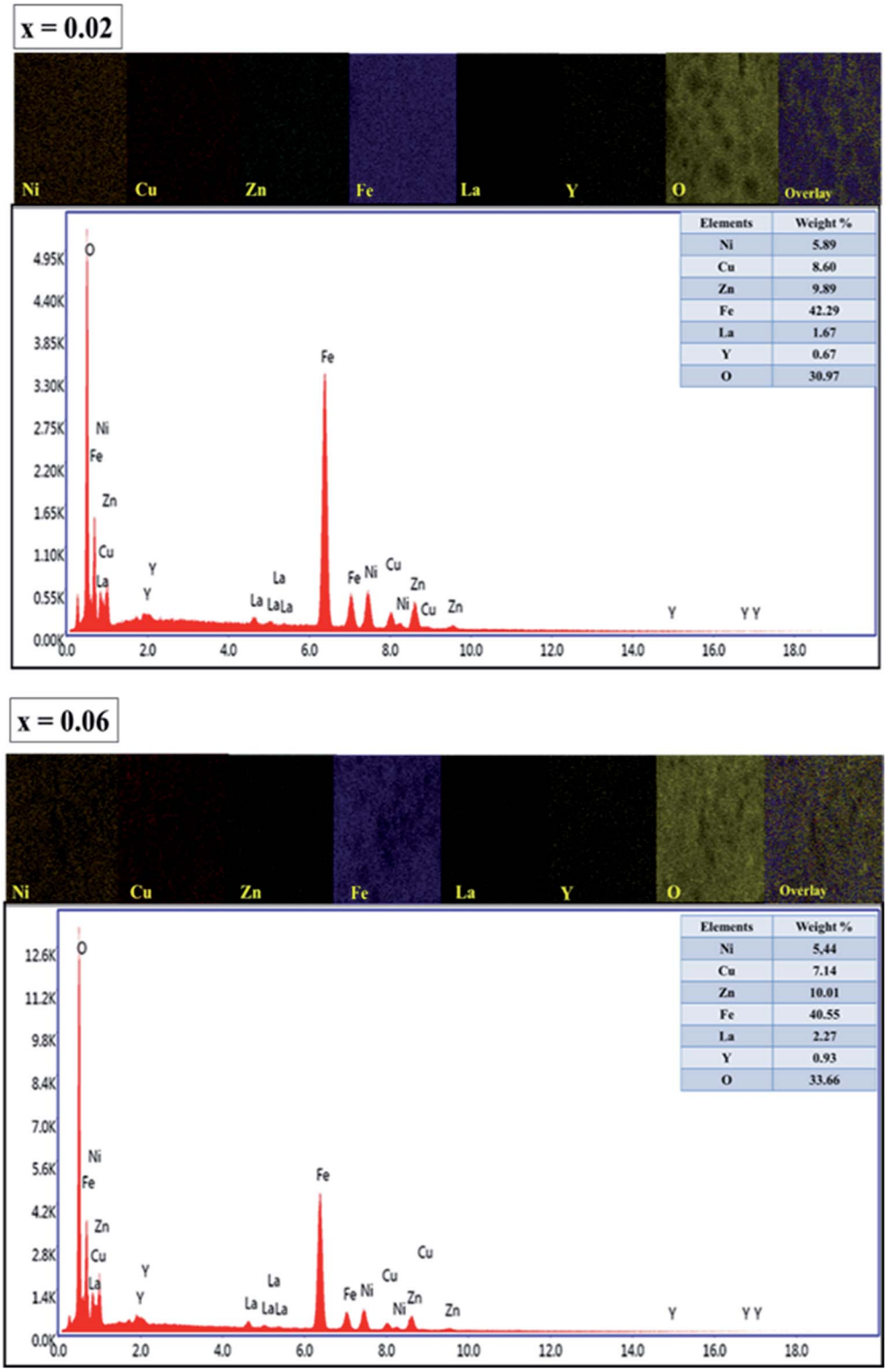

Fig. 3 EDX spectra and elemental mapping of $Ni_{0.4}Cu_{0.2}Zn_{0.4}La_xY_xFe_{2-x}O_4$ ($x = 0.00 - 0.10$) NSFs for $x = 0.02$ and 0.06 compositions.

smaller H_f.[33] The lower covalent behavior of Fe^{3+}–O^{2-} bonds is the reason of greater H_f in A-sites than that in B-sites.[34] The values of I.S. are in the 0.277–0.482 mm s^{-1} characteristics of high spin Fe^{3+} charge state.[35]

The isomer shift of A and B site continuously increased with increasing La^{3+} and Y^{3+} amount. This indicates that the s electron density on both A and B sites decreases with substitution. The quadrupole splitting (Q.S.) occurs because of chemical disorder in the system resulting in an electric field gradient.[35]

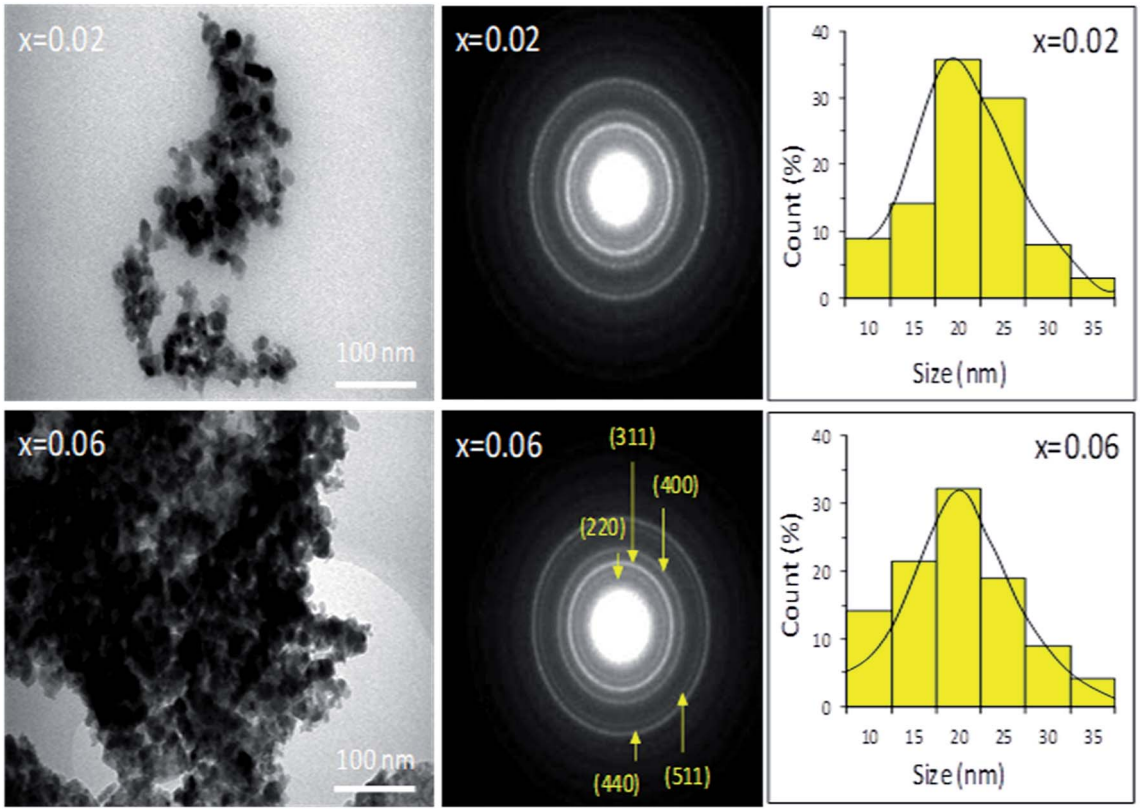

Fig. 4 TEM images, SAED patterns and size histograms of $Ni_{0.4}Cu_{0.2}Zn_{0.4}La_xY_xFe_{2-x}O_4$ (x = 0.00 – 0.10) NSFs for x = 0.02 and 0.06 compositions.

The Q.S. values of A and B sites with respect to substitution are negligible for up to $x = 0.06$. Q.S. is being highest in A site for $x = 0.08$ and 0.10 values. This illustrates a reduction of the cubic symmetry around Fe^{3+} ions with doping. As shown in Table 3, the H_f of iron nuclei at A and B sites decreases with increasing substitutions. This is ascribed to the substitution of magnetic Fe^{3+} (with magnetic moment of 5 μ_B) ions by nonmagnetic La^{3+} and Y^{3+} ions. This provokes a reduction in the superexchange interaction among different ions.

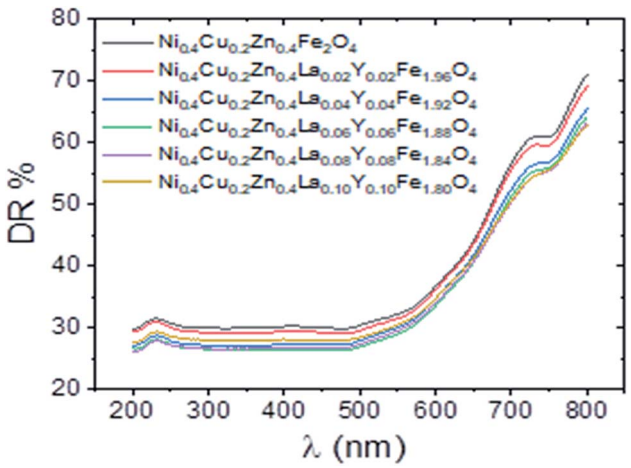

Fig. 5 DR% *vs.* λ spectra of $Ni_{0.4}Cu_{0.2}Zn_{0.4}La_xY_xFe_{2-x}O_4$ (x = 0.00 – 0.10) NPs in 200–800 nm.

3.5. Magnetic properties

Magnetic traits of $Ni_{0.4}Cu_{0.2}Zn_{0.4}La_xY_xFe_{2-x}O_4$ (x = 0.00 – 0.10) NSFs were evaluated using VSM. The experiments of magnetization against applied magnetic field (M–H) of $Ni_{0.4}Cu_{0.2}Zn_{0.4}La_xY_xFe_{2-x}O_4$ (x = 0.00 – 0.10) NSFs were performed at 300 K and 10 K over the field range of ±70 kOe. The results of magnetic hysteresis loops of all products are presented in Fig. 8. From this figure, the magnitudes of M_s, H_c and M_r at both 300 K and 10 K were deduced and listed in Table 4. It is noticed that the various $Ni_{0.4}Cu_{0.2}Zn_{0.4}La_xY_xFe_{2-x}O_4$ (x = 0.00 – 0.10) NSFs show superparamagnetic (SPM) behavior at RT (Fig. 8(a) and (b)). However, the magnetization curve at 10 K (Fig. 8(c) and (d)) illustrates typical character of soft ferromagnetic (FM) nanomaterials characterized by closed hysteresis loops with M_s, M_r and H_c. It is noticed that the M_s of all produced nanoparticles are greater at low temperature than that of RT. For pure $Ni_{0.4}Cu_{0.2}Zn_{0.4}Fe_2O_4$ (x = 0.00) ferrite, M_s magnitude increases from 55.5 emu g^{-1} at 300 K to 88.3 emu g^{-1} at 10 K. The increase in M_s at 10 K compared with RT is ascribed to reduction of the thermal fluctuations and surface spin disorders at the surfaces of the nanoparticles.[36–38] Indeed, the surface spins at high temperatures could be subjected in a short time to many disorder states with similar energies that lead to weaken their responses to the applied field and consequently decreases the magnetization in comparison to their bulk counterpart. Nevertheless, the surface spins can freeze to a certain state below the freezing/blocking temperature, which rises the projection of the moments in the direction of H. Moreover, the coercivity

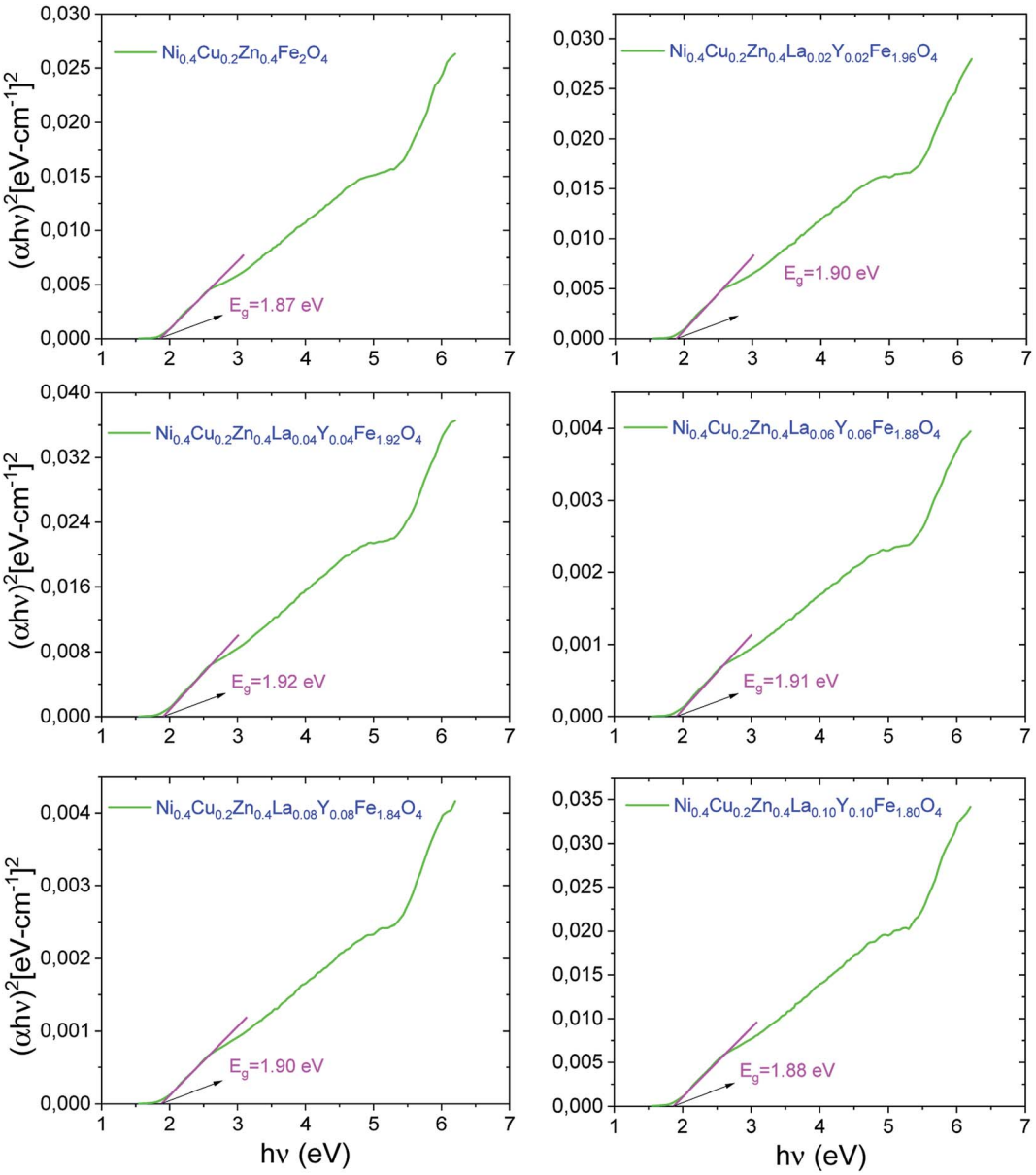

Fig. 6 Tauc plots and extrapolated direct E_g data of $Ni_{0.4}Cu_{0.2}Zn_{0.4}La_xY_xFe_{2-x}O_4$ ($x = 0.00 - 0.10$) NPs.

values of all the products increased at 10 K when compared with 300 K. The enhancement in H_c is ascribed to reduced thermal fluctuations energy at low temperatures that is less efficient in decreasing the effects of magneto-crystalline anisotropy energy.

The pure NiCuZn ferrite displays the highest M_s magnitudes of 55.5 and 88.3 emu g^{-1} at 300 K and 10 K, respectively. These magnitudes agreed very-well with those reported in NiCuZn nanoferrites prepared *via* sol–gel auto-combustion process[39,40] and in NiCuZn thin films.[41] We have observed that there is no improvement in the M_s magnitudes with substitutions. M_s values decrease when the crystallites size reduces with the increase of La^{3+} and Y^{3+} substitution levels.[42,43] Usually, it is ascribed to the surface effects of the magnetic NPs owing to smaller crystallites size, which could be explained by assuming the occurrence of dead magnetic layers because of surface spins disorders.[44] It is anticipated that the number of spins at the surface of different prepared ferrites increases as the crystallites size become smaller. Moreover, the decrease in M_s of NiCuZn ferrites with La^{3+} and Y^{3+} substitutions is considered with the zero magnetic moments of La^{3+} and Y^{3+} ions and their preferential distributions in the octahedral lattice. It is found that the magnetic properties follow the theoretical decrease tendency owing to the replacement of Fe^{3+} ions displaying magnetic moments of 5 μ_B with La^{3+} and Y^{3+} ions having zero magnetic moments. Furthermore, M_s could decrease as a result of reduced exchange interactions among Fe^{3+}–O–Fe^{3+}, which are substituted with the weaker Fe^{3+}–O–La^{3+} and Fe^{3+}–O–Y^{3+} interactions. Consistent with Néel's sublattice model, spinal ferrites exhibit three kinds of interactions among tetrahedral (A) and octahedral (B) sites, *e.g.* A–A, B–B and A–B.[45,46] A–B sublattice

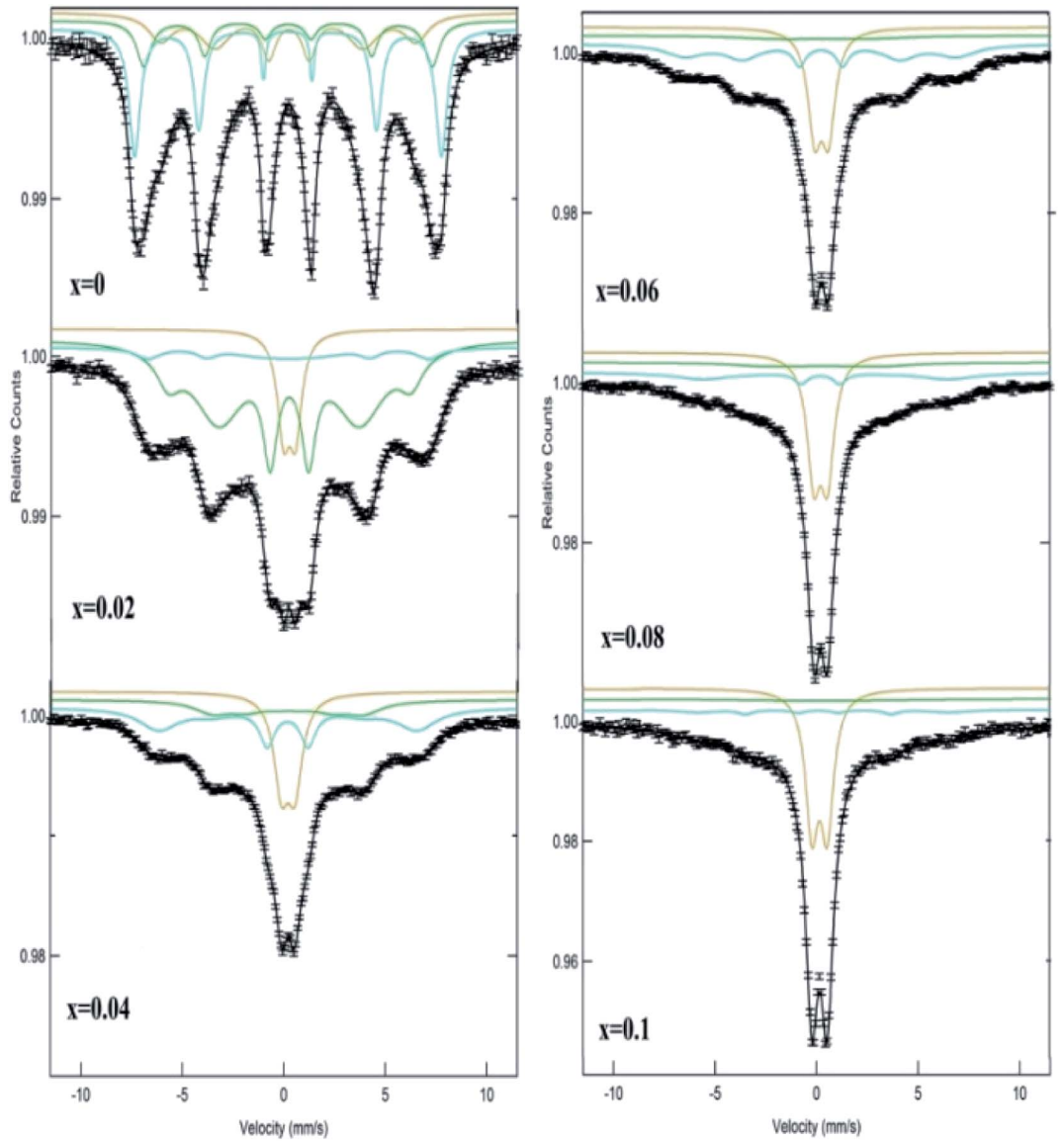

Fig. 7 RT Mössbauer spectra of $Ni_{0.4}Cu_{0.2}Zn_{0.4}La_xY_xFe_{2-x}O_4$ ($x = 0.00 - 0.10$) NSFs.

interaction is the strongest among these three interactions.[44] The total magnetization of doped NiCuZn ferrites is the difference amongst the magnetization of B and A sites. Because of their larger ionic radii, rare earth ions generally occupy the B sites.[47] Hence, the replacement of La^{3+} and Y^{3+} ions having zero magnetic moments at the B sites in NiCuZn ferrite lattices reduces the magnetization. The experimental magnetic moments n_B per unit formula in units of Bohr magneton were determined *via* the following expression:[48,49]

$$n_B = \frac{\text{Molecular weight} \times M_s}{5585}$$

The deduced n_B values were listed in the Table 4. A good agreement between n_B and M_s variation tendency was observed.

The pure NiCuZn ferrite has the highest M_s and n_B values at both RT and 10 K, and then they decrease with increasing the La^{3+} and Y^{3+} substitution contents. The decrease in n_B is owing to the circumstance that the magnetization of the B sites is weakening and, hence, the A–B super-exchange interaction is weakening with La^{3+} and Y^{3+} substitutions, which would then disrupt the structure of collinear spins in the NiCuZn ferrite systems at the B sites.[44] These results are in accordance with Mössbauer results that show a reduction in the super-exchange interaction.

On the other hand, it is noticed from Table 4 that the coercivity of $Ni_{0.4}Cu_{0.2}Zn_{0.4}La_xY_xFe_{2-x}O_4$ ($x = 0.00 - 0.10$) NSFs increases with rising x. Pure NiCuZn NSFs exhibit H_c values of 12.9 (at $T = 300$ K) and 173.2 Oe (at $T = 10$ K), which increase to the 29.2 (at $T = 300$ K) and 452.1 Oe (at $T = 10$ K) for $Ni_{0.4}Cu_{0.2}Zn_{0.4}La_{0.1}Y_{0.1}Fe_{1.8}O_4$ (*i.e.* $x = 0.1$). It is well-known that the H_c and M_s are related by the following expression:[47]

Table 3 Parameters deduced from Mössbauer spectra for $Ni_{0.4}Cu_{0.2}Zn_{0.4}La_xY_xFe_{2-x}O_4$ ($x = 0.00 - 0.10$) NSFs[a]

x	Spectral component	I.S. (±0.01) (mm s^{-1})	Q.S. (±0.02) (mm s^{-1})	H_{hf} (±0.1) (T)	Area (%)
0.00	Sx-A: Fe^{3+}	0.277	0.013	45.212	19.489
	Sx-B_1: Fe^{3+}	0.291	−0.09	42.486	25.434
	Sx-B_2: Fe^{3+}	0.318	−0.027	37.616	55.077
0.02	Sx-A: Fe^{3+}	0.293	−0.002	43.046	37.15
	Sx-B: Fe^{3+}	0.344	0.024	37.071	53.748
	Db: Fe^{3+}	0.341	0.587	—	9.102
0.04	Sx-A: Fe^{3+}	0.305	0.012	39.413	31.88
	Sx-B_1: Fe^{3+}	0.36	−0.051	23.029	42.643
	Db: Fe^{3+}	0.321	0.669	—	25.476
0.06	Sx-A: Fe^{3+}	0.294	−0.024	40.258	28.743
	Sx-B: Fe^{3+}	0.312	0.072	17.227	33.107
	Db: Fe^{3+}	0.327	0.661	—	38.149
0.08	Sx-A: Fe^{3+}	0.441	0.246	37.403	15.79
	Sx-B: Fe^{3+}	0.478	−0.062	19.994	34.129
	Db: Fe^{3+}	0.326	0.673	—	50.081
0.10	Sx-A: Fe^{3+}	0.389	0.202	37.264	7.377
	Sx-B: Fe^{3+}	0.482	0.092	15.442	42.497
	Db: Fe^{3+}	0.327	0.738	—	50.126

[a] (H_{hf}: hyperfine magnetic field. I.S.: isomer shift. Q.S.: quadrupole splitting. W: line width. R_A: relative area).

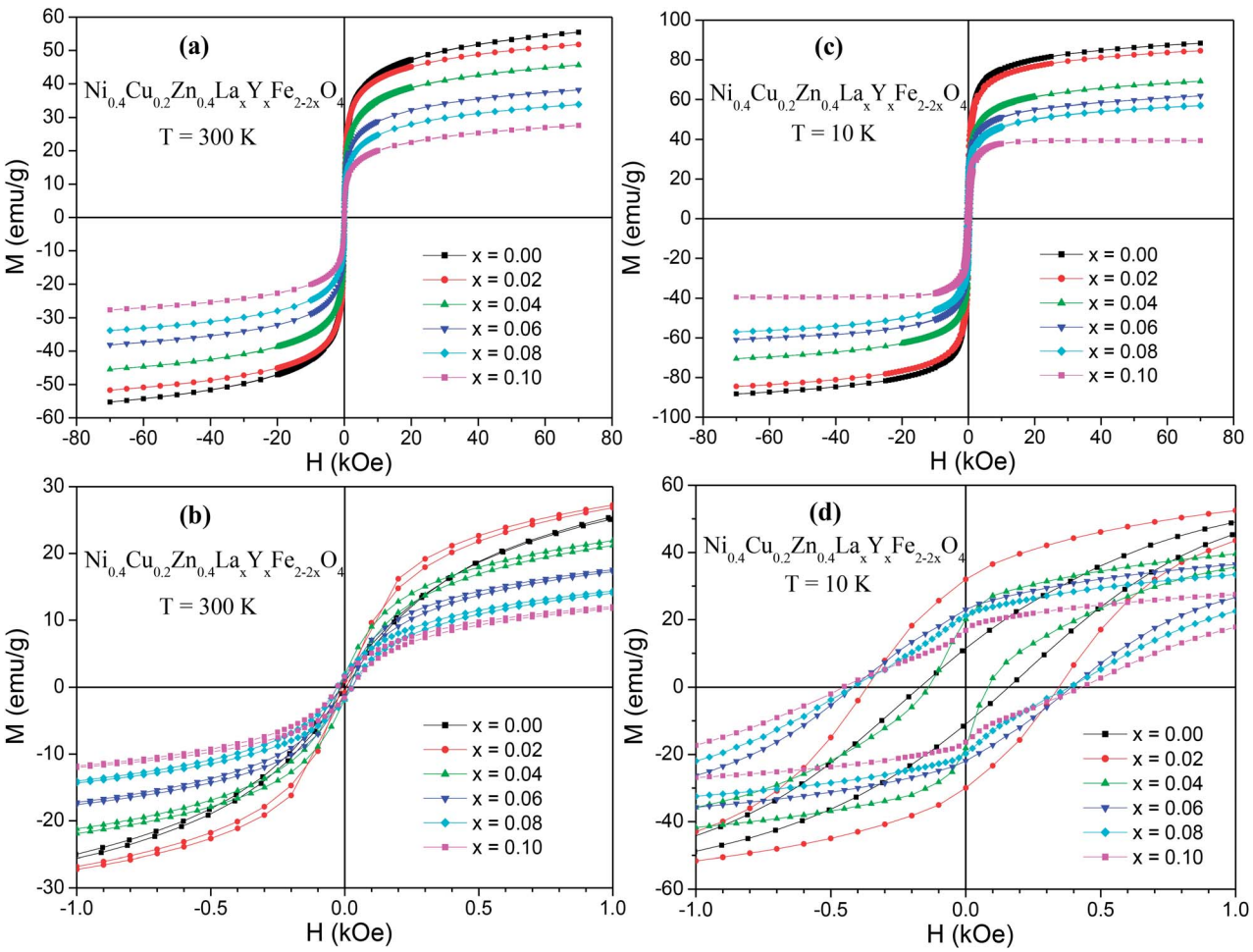

Fig. 8 $M-H$ hysteresis loops of $Ni_{0.4}Cu_{0.2}Zn_{0.4}La_xY_xFe_{2-x}O_4$ ($x = 0.00 - 0.10$) NSFs performed at (a and b) $T = 300$ and (c and d) $T = 10$ K.

Table 4 Magnetic parameters of $Ni_{0.4}Cu_{0.2}Zn_{0.4}La_xY_xFe_{2-x}O_4$ ($x = 0.00 - 0.10$) NSFs deduced from VSM measurements performed at 300 and 10 K

	M_s (emu g^{-1})		M_r (emu g^{-1})		$R = M_r/M_s$		H_c (Oe)		n_B (μ_B)	
x	300 K	10 K	300 K	10 K	300 K	10 K	300 K	10 K	300 K	10 K
0.00	55.5	88.3	0.81	11.9	0.014	0.134	12.9	173.2	2.37	3.76
0.02	51.9	84.7	1.04	32.3	0.020	0.381	9.5	364.4	2.23	3.65
0.04	45.7	69.2	1.92	20.2	0.042	0.292	15.5	138.8	1.99	3.01
0.06	38.2	61.9	1.35	22.8	0.035	0.368	18.2	415.1	1.68	2.72
0.08	33.9	57.0	1.80	21.4	0.053	0.375	28.2	424.6	1.50	2.52
0.10	27.7	39.5	1.60	17.1	0.058	0.433	29.2	452.1	1.24	1.77

$$H_c = \frac{2K}{\mu_0 M_s}$$

where μ_0 is the permeability of free space and K is the magneto-crystalline anisotropy constant. Since M_s was found to decrease with x, the observed increase in coercivity could be a result of the strengthening of the magneto-crystalline anisotropy with La^{3+} and Y^{3+} substitutions.[50,51] Moreover, it is known that H_c and grains size are inversely proportional.[52] Indeed, larger grains offer lesser pinning of domain walls because of the lower volume fractions of grain boundaries.[44] In the present study, it is observed that the crystallites size reduced with La^{3+} and Y^{3+} substitutions. Therefore, the slow improvement of H_c with La^{3+} and Y^{3+} substitutions could be ascribed to the decrease in grains size. The values of squareness ratio "R" at both measurement temperatures are calculated and listed in Table 3. Commonly, the nanoparticles are in multi-magnetic domain (MMD) when $R \geq 0.5$ and in single magnetic domain (SMD) when $R < 0.5$.[53,54] The achieved R values reflect the MD nature at both 300 and 10 K in the prepared spinel ferrites nanoparticles.

3.6. Microwave properties

Microwave properties of $Ni_{0.4}Cu_{0.2}Zn_{0.4}La_xY_xFe_{2-x}O_4$ ($x = 0.00 - 0.10$) NSFs were determined by obtaining reflection losses (RL) spectra of the synthesized NPs between 2 and 18 GHz using coaxial airline. Having measured the S-parameters in vector network analyzer, complex permittivity (ε_r) and permeability (μ_r) values were calculated using material characterization software in this frequency range. Then, normalized input impedence of our NiCuZn NPs were deduced using the complex permittivity and permeability values *via* following eqn.

$$Z_{in} = \sqrt{\mu_r/\varepsilon_r}\,\tan h\left[i(2\pi fd/c)\sqrt{\varepsilon_r\mu_r}\right]$$

here d is the sample thickness, f is the frequency and c is the speed of light. Finally, the reflection loss spectra of each sample were derived using above equation which was determined *via* the transmission line theory for a single layer and metal-backed absorber.

$$RL(dB) = 20\ \log\left|\frac{Z_{in}-1}{Z_{in}+1}\right|$$

Fig. 9 represents the RL spectra of our NSFs in 2–18 GHz interval. There is one RL minima for each sample that is centered between 7 and 10.5 GHz. As amount of doped concentration increases, the frequency at which RL occurs increases slightly. Similarly, microwave absorption capacity enhanced from −28.5 dB to −40 dB. The absorption bandwidth at −10 dB lies between 5 and 8.4 GHz, being wider in highly doped samples (see Table 5). This means that more than 90% of the incoming microwave energy is dissipated within the material in a wide frequency range that is very beneficial feature for good quality absorbers. The optimum doping concentration appeared to be $x = 0.08$ considering both RL and absorption bandwidth parameters.

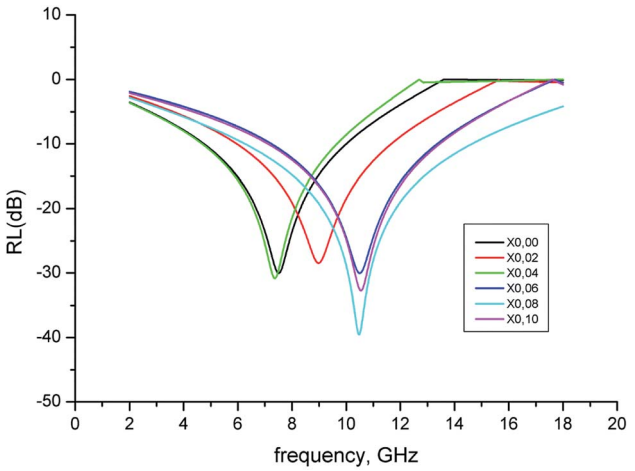

Fig. 9 RL spectra of $Ni_{0.4}Cu_{0.2}Zn_{0.4}La_xY_xFe_{2-x}O_4$ ($x = 0.00 - 0.10$) NSFs.

Table 5 The important parameters reflecting the MW properties of $Ni_{0.4}Cu_{0.2}Zn_{0.4}La_xY_xFe_{2-x}O_4$ ($x = 0.00 - 0.10$) NSFs

x	RL (dB)	f (GHz)	Δf (GHz)
0.00	29.9	7.5	5.3
0.02	28.5	9.0	5.8
0.04	30.8	7.4	5.0
0.06	30.0	10.5	6.2
0.08	39.5	10.5	8.4
0.10	32.6	10.5	6.5

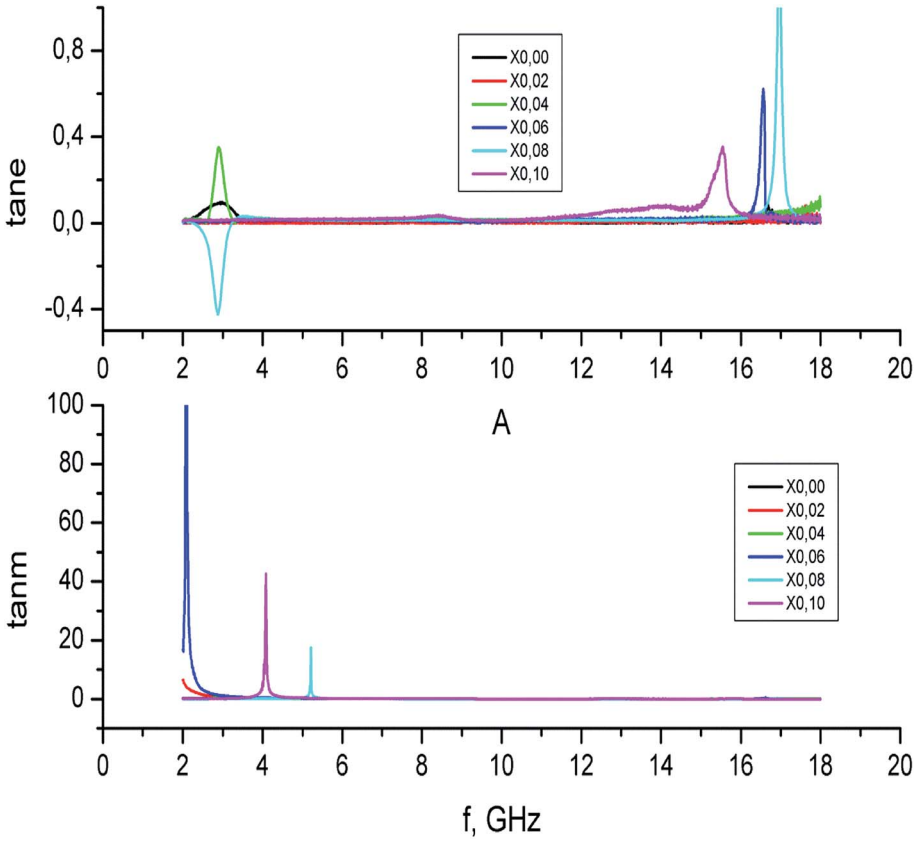

Fig. 10 Dielectric (above) and magnetic (below) loss tangents of $Ni_{0.4}Cu_{0.2}Zn_{0.4}La_xY_xFe_{2-x}O_4$ ($x = 0.00 - 0.10$) NSFs.

Dielectric ($\tan \delta_\varepsilon$) and magnetic ($\tan \delta_\mu$) loss $Ni_{0.4}Cu_{0.2}Zn_{0.4}La_xY_xFe_{2-x}O_4$ ($x = 0.00 - 0.10$) NSFs (Fig. 10). It implies that at low frequencies up to 4 GHz both dielectric and magnetic loss tangents are effective, while at high frequencies between 15 and 17 GHz, only dielectric loss plays role in dissipation. However, in RL spectra, there are no reflection minima at these frequencies meaning that main microwave absorption mechanism was not loss tangents. The possible dissipation mechanism can be explained by dipolar relaxation and spin rotation as follows. The existence of cations with dissimilar valences (Zn^{2+}, Ni^{2+}, Fe^{2+}/Fe^{3+} together with O^{2-}) generates dipoles with diverse strength in the unit cells of LaY doped NiCuZn ferrite NSFs. The conductance loss and dielectric loss are two dominant kinds of energy dissipation as expressed here:

$$\varepsilon'' = \varepsilon''_{\text{relax}} + \frac{\sigma}{\omega\varepsilon_0}$$

where ε_0 is the permittivity of free space, ω is the pulsation, σ is the conductivity, and $\varepsilon''_{\text{relax}}$ is the relaxation polarization. In our case, where the magnetic materials are poor conductors, the crucial mechanism of dielectric loss in absorbing the microwave energy come to be the Debye dipolar relaxation.[55,56] Generally, polycrystalline ferrites have a permeability correlated with two magnetizing mechanisms, *i.e.* domain wall motion and spin rotation.[57,58] The first one is influenced by the size of grains wherein the increase in the size of domain walls will contribute to increase the magnetization. The contribution of the domain walls to the permeability consists of resonance and influenced to frequency.[59] It is effective at lower frequencies below 100 MHz.[56] Instead, the contribution of spin rotation is of resonance that occurs at high frequencies.[60] Therefore, the observed RL minimum around 10 GHz can also be explained dissipation due to the spin rotation. According to the obtained results, one can claim that the $Ni_{0.4}Cu_{0.2}Zn_{0.4}La_xY_xFe_{2-x}O_4$ ($x = 0.00 - 0.10$) NSFs could be utilized as radar absorbing materials in X-band due to the high RL and large absorbing bandwidth.

4. Conclusion

The influence of La–Y substitution on the structure, optical, magnetic and microwave properties of NiCuZn NSFs on were investigated in detail. With raising the amount of La–Y, the lattice parameters and crystallite size increase due the enlargement of crystal. Tauc plots assign direct and allowed electronic transitions for all NiCuZn mixed nanoferrite samples. E_g values in a range of 1.87 eV–1.92 eV also reveal the semiconducting nature of nanoferrite samples. La^{3+} and Y^{3+} ions substitution process with $x = 0.02 - 0.10$ concentrations slightly increased the order of E_g data. The Mössbauer results revealed that the hyperfine field at A and B sites decreases with substitution of La^{3+} and Y^{3+} in Fe^{3+} because of the replacement of magnetic Fe^{3+} (with magnetic moment of 5 μ_B) ions by nonmagnetic La^{3+} and Y^{3+} ions. The magnetic properties of various nanoparticles were analyzed at $T = 300$ K and 10 K. All

prepared nanoparticles exhibit superparamagnetic behavior at RT and soft ferromagnetic trait at 10 K. It is noticed that the deduced magnetic parameters of all the produced nanoparticles are higher at low temperature than that of RT, owing to the reduced thermal fluctuations and surface spin disorders at the surfaces of the nanoparticles. It is observed that M_s and M_r decrease and H_c increases slightly with La^{3+} and Y^{3+} substitutions. The reduction in magnetization is attributed to reduction in crystallites size, zero magnetic moments of La^{3+} and Y^{3+} ions substituting magnetic. Microwave characterization of $Ni_{0.4}Cu_{0.2}Zn_{0.4}La_xY_xFe_{2-x}O_4$ ($x = 0.00 - 0.10$) NSFs showed that RL occurs at different frequencies between 7.5 and 10.5 GHz. The LaY doping shifted the RL minimum to higher frequencies. Besides, absorption bandwidth increased with LaY amount reaching to 8.4 GHz @ 10 GHz in $x = 0.08$ sample. Also, this product has the better microwave capability with RL of −40 dB @ 10.5 GHz. Therefore, the $Ni_{0.4}Cu_{0.2}Zn_{0.4}La_xY_xFe_{2-x}O_4$ ($x = 0.00 - 0.10$) NSFs could be utilized as radar absorbing materials in X-band due to the high RL and large absorbing bandwidth.

Conflicts of interest

There are no conflicts to declare.

References

1 G. Gan, H. Zhang, Q. Li, J. Li, X. Huang, F. Xie, *et al.*, Low loss, enhanced magneto-dielectric properties of Bi_2O_3 doped Mg–Cd ferrites for high frequency antennas, *J. Alloys Compd.*, 2018, **735**, 2634.

2 K. K. Kefeni, T. A. Msagati and B. B. Mamba, Ferrite nanoparticles: synthesis, characterisation and applications in electronic device, *Mater. Sci. Eng., B*, 2017, **215**, 37.

3 D.-H. Kim, H. Zeng, T. C. Ng and C. S. Brazel, T1 and T2 relaxivities of succimer-coated MFe_2O_4 (M = Mn^{2+}, Fe^{2+} and Co^{2+}) inverse spinel ferrites for potential use as phase-contrast agents in medical MRI, *J. Magn. Magn. Mater.*, 2009, **321**, 3899.

4 J. Lu, S. Ma, J. Sun, C. Xia, C. Liu, Z. Wang, *et al.*, Manganese ferrite nanoparticle micellar nanocomposites as MRI contrast agent for liver imaging, *Biomaterials*, 2009, **30**, 2919.

5 V. Pilati, R. Cabreira Gomes, G. Gomide, P. Coppola, F. G. Silva, FbL. Paula, *et al.*, Core/shell nanoparticles of non-stoichiometric Zn–Mn and Zn–Co ferrites as thermosensitive heat sources for magnetic fluid hyperthermia, *J. Phys. Chem. C*, 2018, **122**, 3028.

6 N. Sanpo, C. C. Berndt, C. Wen and J. Wang, Transition metal-substituted cobalt ferrite nanoparticles for biomedical applications, *Acta Biomater.*, 2013, **9**, 5830.

7 I. Sharifi, H. Shokrollahi and S. Amiri, Ferrite-based magnetic nanofluids used in hyperthermia applications, *J. Magn. Magn. Mater.*, 2012, **324**, 903.

8 M. D. Shultz, S. Calvin, P. P. Fatouros, S. A. Morrison and E. E. Carpenter, Enhanced ferrite nanoparticles as MRI contrast agents, *J. Magn. Magn. Mater.*, 2007, **311**, 464.

9 C. Singh, A. Goyal and S. Singhal, Nickel-doped cobalt ferrite nanoparticles: efficient catalysts for the reduction of nitroaromatic compounds and photo-oxidative degradation of toxic dyes, *Nanoscale*, 2014, **6**, 7959.

10 K. Ramakrishna, C. Srinivas, B. Tirupanyam, P. Ramesh, S. Meena, D. Potukuchi, *et al.*, Effect of Cu^{2+} substitution on the magnetic properties of co-precipitated Ni–Cu–Zn ferrite nanoparticles, *AIP Conf. Proc.*, 2017, **1832**, 050154.

11 M. P. Reddy, W. Madhuri, N. R. Reddy, K. V. S. Kumar, V. R. K. Murthy and R. R. Reddy, Influence of copper substitution on magnetic and electrical properties of MgCuZn ferrite prepared by microwave sintering method, *Mater. Sci. Eng., C*, 2010, **30**, 1094.

12 S. More, R. Kadam, A. Kadam, D. Mane and G. Bichile, Structural properties and magnetic interactions in Al^{3+} and Cr^{3+} co-substituted $CoFe_2O_4$ ferrite, *Open Chem.*, 2010, **8**, 419.

13 X. C. Zhong, X. J. Guo, S. Y. Zou, H. Y. Yu, Z. W. Liu, Y. F. Zhang, *et al.*, Improving soft magnetic properties of Mn–Zn ferrite by rare earth ions doping, *AIP Adv.*, 2017, **8**, 047807.

14 R. Tholkappiyan and K. Vishista, Influence of lanthanum on the optomagnetic properties of zinc ferrite prepared by combustion method, *Phys. B*, 2014, **448**, 177.

15 R. Kershi, F. Ali and M. Sayed, Influence of rare earth ion substitutions on the structural, optical, transport, dielectric, and magnetic properties of superparamagnetic iron oxide nanoparticles, *J. Adv. Ceram.*, 2018, **7**, 218.

16 J. Hu and M. Yan, Preparation of high-permeability NiCuZn ferrite, *J. Zhejiang Univ., Sci., B*, 2005, **6**, 580.

17 S. M. Kabbur, U. R. Ghodake, R. C. Kambale, S. D. Sartale, L. P. Chikhale and S. S. Suryavanshi, Magnetic, Electric and Optical Properties of Mg-Substituted Ni–Cu–Zn Ferrites, *J. Electron. Mater.*, 2017, **46**, 5693.

18 T. Krishnaveni, B. R. Kanth, V. S. R. Raju and S. R. Murthy, Fabrication of multilayer chip inductors using Ni–Cu–Zn ferrites, *J. Alloys Compd.*, 2006, **414**, 282.

19 M. M. Eltabey, K. M. El-Shokrofy and S. A. Gharbia, Enhancement of the magnetic properties of Ni–Cu–Zn ferrites by the non-magnetic Al^{3+}-ions substitution, *J. Alloys Compd.*, 2011, **509**, 2473.

20 H. Harzali, F. Saida, A. Marzouki, A. Megriche, F. Baillon, F. Espitalier, *et al.*, Structural and magnetic properties of nano-sized NiCuZn ferrites synthesized by co-precipitation method with ultrasound irradiation, *J. Magn. Magn. Mater*, 2016, **419**, 50.

21 H. Harzali, F. Baillon, O. Louisnard, F. Espitalier and A. Mgaidi, Sono-crystallization of $ZnSO_4 \cdot 7H_2O$ with variation of solution heights, *Chem. Eng. J.*, 2012, **195**, 332.

22 M. A. Almessiere, Y. Slimani, A. D. Korkmaz, H. Gungunes, M. Nawaz, S. E. Shirsath, A. Baykal and I. Ercan, Ca^{2+}/Mg^{2+} co-substituted strontium nanohexaferrites: magnetic investigation and Mossbauer analysis, *J. Sol-Gel Sci. Technol.*, 2019, **92**, 239–251.

23 A. Sadaqat, M. Almessiere, Y. Slimani, S. Guner, M. Sertkol, H. Albetran, A. Baykal, S. E. Shirsath, B. Ozcelik and I. Ercan, Structural, optical and magnetic properties of Tb^{3+} substituted Co nanoferrites prepared *via* sonochemical

approach, *Ceram. Int.*, 2019, DOI: 10.1016/j.ceramint.2019.07.280.

24 S. E. Shirsath, D. Wang, S. S. Jadhav, M. L. Mane, and S. Li, Ferrites obtained by sol–gel method, ed. L. Klein, M. Aparicio and A. Jitianu, *Handbook of Sol–Gel Science and Technology*, Springer, Cham, 2018, pp. 695–735.

25 W. Wei, W. Ye, J. Wang, C. Huang, J.-B. Xiong, H. Qiao, S. Cui and L. Mi, Hydrangea-like α-$Ni^{1/3}Co^{2/3}(OH)_2$ Reinforced by Ethyl Carbamate"Rivet" for All-Solid-State Supercapacitors with Outstanding Comprehensive Performance, *ACS Appl. Mater. Interfaces*, 2019, **11**(35), 32269–32281.

26 W. Wei, W. Chen, L. Ding, S. Cui and L. Mi, Construction of hierarchical three-dimensional interspersed flower-like nickel hydroxide for asymmetric super capacitors, *Nano Res.*, 2017, **10**(11), 3726–3742.

27 W. Wei, J. Wu, S. Cui, Y. Zhao, W. Chen and L. Mi, α-$Ni(OH)_2$/$NiS_{1.97}$ heterojunction composites with excellent ion and electron transport properties for advanced super capacitors, *Nanoscale*, 2019, **11**, 6243–6253.

28 J. Tauc, R. Grigorovici and A. Vancu, Optical properties and electronic structure of amorphous germanium, *Phys. Status Solidi*, 1966, **15**, 627.

29 A. D. Korkmaz, S. Güner, Y. Slimani, H. Gungunes, Md. Amir, A. Manikandan and A. Baykal, Microstructural, optical, and magnetic properties of vanadium-substituted nickel spinel nanoferrites, *J. Supercond. Novel Magn.*, 2019, **32**, 1057.

30 M. A. Almessiere, Y. Slimani, A. D. Korkmaz, S. Guner, M. Sertkol, S. E. Shirsath and A. Baykal, Structural, optical and magnetic properties of Tm^{3+} substituted cobalt spinel ferrites synthesized *via* sonochemical approach, *Ultrason. Sonochem.*, 2019, **54**, 1.

31 Y. Slimani, M. A. Almessiere, M. Nawaz, A. Baykal, S. Akhtar, I. Ercan and I. Belenli, Effect of bimetallic (Ca, Mg) substitution on magneto-optical properties of $NiFe_2O_4$ nanoparticles, *Ceram. Int.*, 2019, **45**, 6021.

32 Y. Slimani, M. A. Almessiere, M. Sertkol, S. E. Shirsath, A. Baykal, M. Nawaz, S. Akhtar, B. Ozcelik and I. Ercan, Structural, magnetic, optical properties and cation distribution of nanosized $Ni_{0.3}Cu_{0.3}Zn_{0.4}Tm_xFe_{2-x}O_4$ ($0.0 \leq x \leq 0.10$) spinel ferrites synthesized by ultrasound irradiation, *Ultrason. Sonochem.*, 2019, **57**, 203.

33 L. George, C. Viji, H. Mathew and E. M. Mohammed, Structural, Dielectric, Magnetic and Optical Properties of Cerium Substituted Ni–Zn Mixed Ferrite, *Mater. Sci. Res. India*, 2017, **14**, 133.

34 R. J. Joseyphus, A. Narayanasamy, K. Shinoda, B. Jeyadevan and K. Tohji, Synthesis and magnetic properties of the size-controlled Mn–Zn ferrite nanoparticles by oxidation method, *J. Phys. Chem. Solids*, 2006, **67**, 1510.

35 A. Lakshman, P. S. V. Subba Rao and K. H. Rao, Mössbauer spectroscopic analyses of $Mg_{0.9}Cu_{0.1}Mn_{0.05}Cr_xFe_{1.95-x}O_4$ spinel ferrites, *Mater. Lett.*, 2006, **60**, 7.

36 H. Kumar, R. C. Srivastava, j. P. Singh, P. Negi, H. M. Agrawal, D. Das and K. H. Chae, Structural and magnetic study of dysprosium substituted cobalt ferrite nanoparticles, *J. Magn. Magn. Mater.*, 2016, **401**, 16.

37 M. A. Almessiere, Y. Slimani, S. Güner, J. van Leusen, A. Baykal and P. Kögerler, Effect of Nb^{3+} ion substitution on the magnetic properties of $SrFe_{12}O_{19}$ hexaferrites, *J. Mater. Sci.: Mater. Electron.*, 2019, **30**, 11181.

38 M. A. Almessiere, Y. Slimani, H. Gungunes, A. Manikandan and A. Baykal, Investigation of the effects of Tm^{3+} on the structural, microstructural, optical, and magnetic properties of Sr hexaferrites, *Results Phys.*, 2019, **13**, 102166.

39 M. A. Almessiere, Y. Slimani, H. S. El Sayed and A. Baykal, Morphology and magnetic traits of strontium nanohexaferrites: effects of manganese/yttrium co-substitution, *J. Rare Earths*, 2019, **37**, 732–740.

40 V. Chaudhari, S. E. Shirsath, M. L. Mane, R. H. Kadam, S. B. Shelke and D. R. Mane, Crystallographic, magnetic and electrical properties of $Ni_{0.5}Cu_{0.25}Zn_{0.25}La_xFe_{2-x}O_4$ nanoparticles fabricated by sol–gel method, *J. Alloys Compd.*, 2013, **549**, 213.

41 P. K. Roy and J. Bera, Electromagnetic properties of samarium-substituted NiCuZn ferrite prepared by auto-combustion method, *J. Magn. Magn. Mater.*, 2009, **321**, 247.

42 F. Liu, C. Yang, T. Ren, A. Z. Wang, J. Yu and L. Liu, NiCuZn ferrite thin films grown by a sol–gel method and rapid thermal annealing, *J. Magn. Magn. Mater.*, 2007, **309**, 75.

43 M. A. Almessiere, Y. Slimani, S. Güner, A. Baykal and I. Ercan, Effect of dysprosium substitution on magnetic and structural properties of $NiFe_2O_4$ nanoparticles, *J. Rare Earths*, 2019, **37**, 871.

44 M. A. Almessiere, Y. Slimani, S. Güner, M. Nawaz, A. Baykal, F. Aldakheel, S. Akhtar, I. Ercan, İ. Belenli and B. Ozçelik, Magnetic and structural characterization of Nb^{3+}-substituted $CoFe_2O_4$ nanoparticles, *Ceram. Int.*, 2019, **45**, 8222.

45 C. Murugesan and G. Chandrasekaran, Impact of Gd^{3+} substitution on the structural, magnetic and electrical properties of cobalt ferrite nanoparticles, *RSC Adv.*, 2015, **5**, 73714.

46 M. A. Almessiere, Y. Slimani, S. Guner, M. Nawaz, A. Baykal, F. Aldakheel, A. Sadaqat and I. Ercan, Effect of Nb substitution on magneto-optical properties of $Co_{0.5}Mn_{0.5}Fe_2O_4$ nanoparticles, *J. Mol. Struct.*, 2019, **1195**, 269.

47 M. A. Almessiere, Y. Slimani, M. Sertkol, F. A. Khan, M. Nawaz, H. Tombuloglu, E. A. Al-Suhaimi and A. Baykal, Ce–Nd Co-substituted nanospinel cobalt ferrites: an investigation of their structural, magnetic, optical, and apoptotic properties, *Ceram. Int.*, 2019, **45**, 16147.

48 M. A. Almessiere, A. D. Korkmaz, Y. Slimani, M. Nawaz, S. Ali and A. Baykal, Magneto-optical properties of Rare Earth metals substituted Co–Zn spinel nanoferrites, *Ceram. Int.*, 2019, **45**, 3449.

49 M. A. Almessiere, Y. Slimani, U. Kurtan, S. Guner, M. Sertkol, S. E. Shirsath, S. Akhtar, A. Baykal and I. Ercan, Structural, magnetic, optical properties and cation distribution of nanosized $Co_{0.7}Zn_{0.3}Tm_xFe_{2-x}O_4$ ($0.0 \leq x \leq 0.04$) spinel ferrites synthesized by ultrasonic irradiation, *Ultrason. Sonochem.*, 2019, **58**, 104638.

50 M. A. Almessiere, Y. Slimani, A. D. Korkmaz, N. Taskhandi, M. Sertkol, A. Baykal, S. E. Shirsath, İ. Ercan and B. Ozçelik, Sonochemical synthesis of Eu^{3+} substituted $CoFe_2O_4$ nanoparticles and their structural, optical and magnetic properties, *Ultrason. Sonochem.*, 2019, **5**, 104621.

51 M. A. Almessiere, Y. Slimani, M. Sertkol, M. Nawaz, A. Sadaqat, A. Baykal, I. Ercan, B. Ozçelik and B. Ozçelik, Effect of Nb^{3+} Substitution on the Structural, Magnetic, and Optical Properties of $Co_{0.5}Ni_{0.5}Fe_2O_4$ Nanoparticles, *Nanomaterials*, 2019, **9**, 430.

52 M. A. Almessiere, Y. Slimani, A. Demir Korkmaz, M. Sertkol, A. Baykal, I. Ercan and B. Özçelik, Sonochemical Synthesis of $CoFe_{2-x}Nd_xO_4$ Nanoparticles: Structural, Optical, and Magnetic Investigation, *J. Supercond. Novel Magn.*, 2019, 1–8.

53 Y. Slimani, M. A. Almessiere, S. Güner, N. A. Tashkandi, A. Baykal, M. F. Sarac, M. Nawaz and I. Ercan, Calcination effect on the magneto-optical properties of vanadium substituted $NiFe_2O_4$ nanoferrites, *J. Mater. Sci.: Mater. Electron.*, 2019, **30**, 9143.

54 M. A. Almessiere, Y. Slimani, S. Guner, M. Sertkol, A. Demir Korkmaz, S. E. Shirsath and A. Baykal, Sonochemical Synthesis and Physical Properties of $Co_{0.3}Ni_{0.5}Mn_{0.2}Eu_xFe_{2-x}O_4$ nano-spinel ferrites, *Ultrason. Sonochem.*, 2019, **58**, 104654.

55 S. He, G.-S. Wang, C. Lu, J. Liu, B. Wen, H. Liu, L. Guo and M.-S. Cao, Enhanced wave absorption of nanocomposites based on the synthesized complex symmetrical CuS nanostructure and poly(vinylidene fluoride), *J. Mater. Chem. A*, 2013, **1**, 4685.

56 D. Chen, H. Quan, G. S. Wang and L. Guo, Hollow α-MnS Spheres and Their Hybrids with Reduced Graphene Oxide: Synthesis, Microwave Absorption, and Lithium Storage Properties, *ChemPlusChem*, 2013, **78**, 843.

57 S. Chikazumi, *Physics of Ferromagnetism (International Series of Monographs on Physics, Book 94)*, Oxford University Press, 2nd edn, 2009, ISBN-10:0199564817.

58 D. Stoppels, Developments in soft magnetic power ferrites, *J. Magn. Magn. Mater.*, 1996, **160**, 323.

59 T. Nakamura, T. Miyamoto and Y. Yamada, Complex permeability spectra of polycrystalline Li–Zn ferrite and application to EM-wave absorber, *J. Magn. Magn. Mater.*, 2003, **256**, 340.

60 G. T. Rado, R. W. Wright and W. H. Emerson, Ferromagnetism at very high frequencies. III. Two mechanisms of dispersion in a ferrite, *Phys. Rev.*, 1950, **80**, 273.